Supporting Information

Bipolar Conjugated Microporous Polymer Anchored Graphene Hybrids Towards High-Performance Zinc−Organic Batteries

Chengmin Hu[a], Yumin Chen[a], Ziyang Song[a], Ling Miao[a,*], Hui Duan[a,*], Yaokang Lv[b], Li Xie[c,d], Mingxian Liu [a,*] and Lihua Gan[a,*]

[a] Shanghai Key Lab of Chemical Assessment and Sustainability, School of Chemical Science and Engineering, Tongji University, Shanghai 200092, P. R. China.

E-mail: 22169@tongji.edu.cn, dhui@tongji.edu.cn, liumx@tongji.edu.cn, ganlh@tongji.edu.cn

[b] College of Chemical Engineering, Zhejiang University of Technology, Hangzhou 310014, P. R. China.

[c] Key Laboratory of Yangtze River Water Environment Ministry of Education, College of Environmental Science and Engineering, Tongji University, Shanghai 200092, P. R. China.

[d] Shanghai Institute of Pollution Control and Ecological Security, Shanghai 200092, P. R. China.

Table of Contents

1.1 Materials Synthesis.

Preparation of GO and CMPs.

GO was synthesized *via* the modified Hummers method[S1]. GO (2.5 mg mL^{-1}) aqueous solutions were prepared by adding 500 mg as-synthesized GO powders into 200 mL H_2O, the solutions were treated for 2 hours of ultrasound.

Following our previous reports[S2], briefly, 1.43 g (6 mmol) 2,6-diaminoanthraquinone (DAQ) dissolved in 50 mL of N, N-Dimethylformamide (DMF) is slowly added dropwise to a mixture of 0.62 g (2.5 mmol) of tetrachloro-1,4-benzoquinone (TBQ) and 30 mL of DMF to a 100 mL Teflon–lined stainless–steel autoclave, the autoclave was hydrothermally at 160 °C for 10 mins, 0.5h, 1h and 24 h, then naturally cooled to room temperature. After the reaction, the mixtures were filtered over a 0.22 μm PTFE membrane to get the crude product. And then wash with ethanol (500 mL×3), N, N-dimethylformamide (500 mL×3) and deionized water (500 mL×3) to remove unreacted raw materials. The production yield is about 62 %, named CMPs.

Preparation of rGO@CMPs Hybrids.

The as-synthesized CMPs were dispersed into H_2O to obtain a 2.5 mg mL^{-1} suspension. To a 100 mL Teflon-lined stainless steel autoclave, GO solution and CMPs suspension were added in 20, 30 and 40% mass ratios. After cooling naturally to room temperature, freeze-drying was performed to obtain the rGO@CMPs hybrid material. Throughout the paper, the 30% mass ratio of GO and CMPs is chosen as the optimal sample unless otherwise noted. Pristine rGO was synthesized by 80 mL GO solution without CMPs for hydrothermal treatment as a reference.

1.2 Characterization.

The sample morphology was observed by field-emission scanning electron microscopy (SEM, Hitachi S-4800) and transmission electron microscopy (TEM, JEM-2100). The elemental mapping characterization was carried out on a JEM-F200 instrument equipped with an energy diffraction system. Fourier-transformed infrared spectrum (FT-IR) was collected through a Thermo Nicolet NEXUS spectrometer. X-ray diffraction test was performed to analyze the material structure using X-ray diffraction (XRD, Bruker D8 advance powder diffractometer with a Cu Kα radiation source). X-ray photoelectron spectrometer (XPS, AXIS Ultra DLD) was utilized to study the surface chemistry of the samples.

Nitrogen sorption characterization was performed through a Micromeritics ASAP2020 physisorption analyzer at −196 °C to calculate the Brunauer–Emmert–Teller (BET) surface area, pore volume, and pore size distribution. The surface area and pore size distribution were obtained by using the BET equation and the nonlocal density functional theory model. The ultraviolet-visible (UV-Vis) spectra were obtained with a JASCO V-750 UV-Vis spectrometer. For ex-situ spectroscopic characterizations including XPS and SEM, the organic cathodes were collected by disassembling the batteries at specific voltages during (dis)charging. After that, the electrodes were rinsed thoroughly with distilled water for 5 times to guarantee the removal of adhered glass fiber and residual electrolyte. Finally, the electrodes were dried in a vacuum oven at 60 °C for 24 h.

Electrochemical Measurements.

The resulting rGO@CMPs composite material is prepared into a positive electrode material by following steps, firstly, active material (rGO, CMPs and rGO@CMPs), conductive graphite (conductive agent), polytetrafluoroethylene (binder) were added into the glass bottles at a mass ratio of 7.5:1.5:1, after that, the appropriate amount of ethanol was added to disperse the slurry by ultrasonic treatment, and then it was dried at 80 °C to remove the excess ethanol. The obtained mud is rolled into a disc by a 20 MPa tablet press and loaded on stainless steel mesh, then the positive electrode material is obtained by vacuum drying for 12 h. The mass load of rGO@CMPs on the positive pole is about 2 mg cm^{-2}. A 2032 button aqueous zinc organic battery (ZOBs) was constructed using commercial zinc foil as anode and 2 mol L^{-1} $Zn(CF_3SO_3)_2$ as electrolyte. We gradually increase the mass load on the positive electrode to 5, 10, 20 mg cm^{-2}, and test its practical application prospect. The galvanostatic charge/discharge (GCD), rate performance, and cycle stability were tested on a LAND-CT3001A battery test system with a voltage range of 0.0 − 1.8 V. The cyclic voltammetry (CV) and electrochemical impedance spectroscopy (EIS) measurements with an amplitude of 0.005 V and a test frequency of 10^{-2}~10^{6} H_Z were characterized on a CHI660E electrochemical workstation. The equivalent circuit of Nyquist plots includes the equivalent series resistance (R_s), charge transfer resistance (R_{ct}), Warburg impedance (Z_w) and constant phase angle element (CPE). Galvanostatic charge/discharge (GCD) measurements were conducted on the CT3001A battery test system in the potential range of 0−1.8 V. The specific capacity (C_m, mAh g^{-1}) was determined from GCD

profiles using the following form:

$$Cm = \frac{I \times \Delta t}{m} \quad \text{(Eq. S1)}$$

where I, Δt, m refer to the current density (A g^{-1}), the discharging time (s) and the mass loading of active materials on the cathode, respectively.

The gravimetric energy density (E, Wh kg^{-1}) and power density (P, W kg^{-1}) of ZIHCs were estimated based on the following forms:

$$E = C_m \times \Delta V \quad \text{(Eq. S2)}$$

$$P = \frac{E}{1000 \times \Delta t} \quad \text{(Eq. S3)}$$

where ΔV is the voltage window.

The normalized of $C'(\omega)$ and $C''(\omega)$ as a function of frequency in the complex model, which is

$$C(\omega) = C'(\omega) - jC''(\omega) \quad \text{(Eq. S4)}$$

where $C'(\omega)$ and $C''(\omega)$ are the imaginary and real parts of the capacitance, respectively[S3].

1.3 Density Functional Theory.

The theoretical calculations were executed via the Gaussian 16 suite of programs[S4]. The CMPs structural unit and rGO bilayer structure were optimized at the wb97XD/6-31+G(d) level of theory. The RDG analysis[S5] was carried out with Multiwfn program[S6], where RDG value offers the interaction strength and sign($\lambda_2\rho$) value shows interaction types. Large and negative values of sign($\lambda_2\rho$) are suggestive of H-bond interactions, values near zero unravel the π–π stacking interactions. Moreover, the corresponding gradient isosurface was colored, which can intuitively display the interaction region and strength. The non-covalent interaction (NCI) maps were plotted using VMD software[S7]. The molecular orbital energy levels, including the lowest unoccupied molecular orbital (LUMO) and the highest occupied molecular orbital (HOMO) were analyzed at the B3LYP-D3/TZVP level of theory.

Section S2. Supporting Characterizations

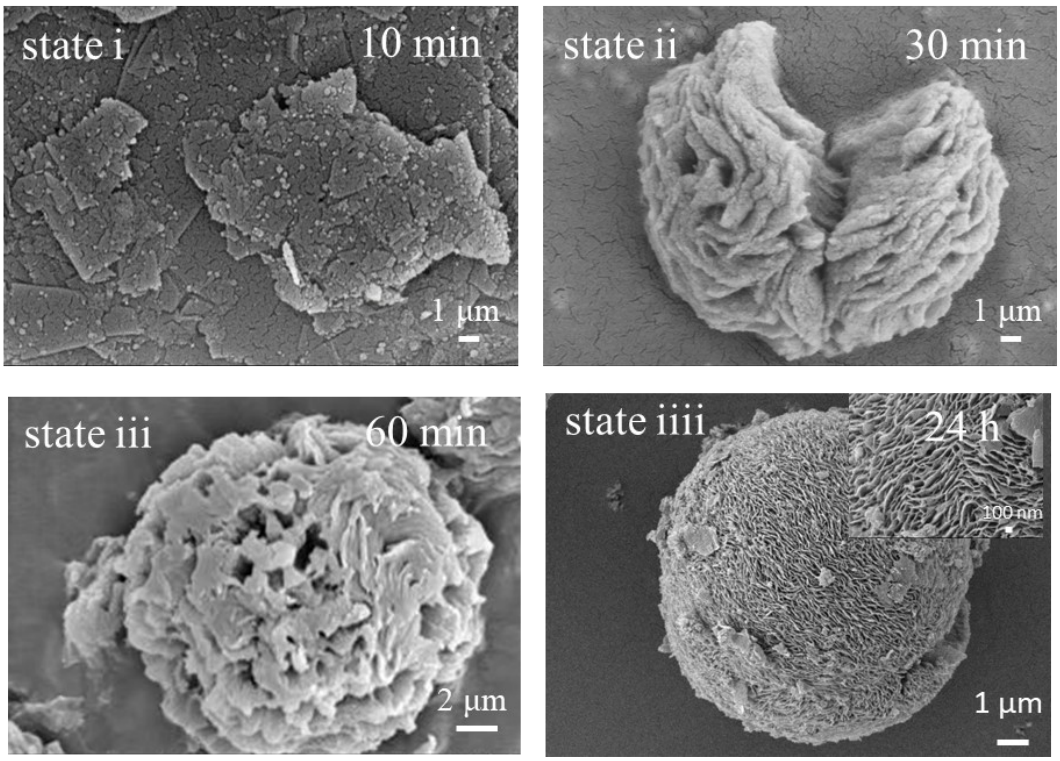

Figure S1. SEM images of TBQ and DAQ reactions after 10 min, 30 min, 60 min and 24h.

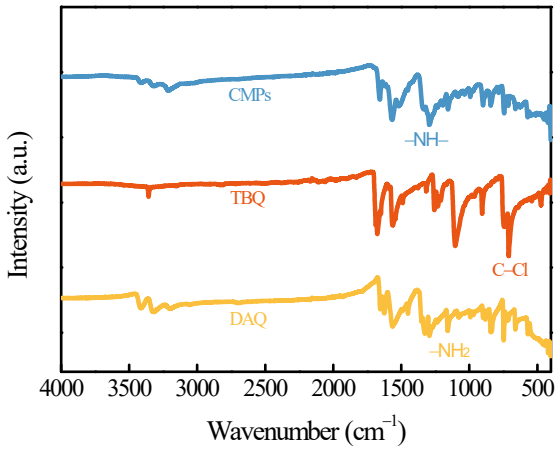

Figure S2. FT-IR spectra of CMPs, TBQ and DAQ.

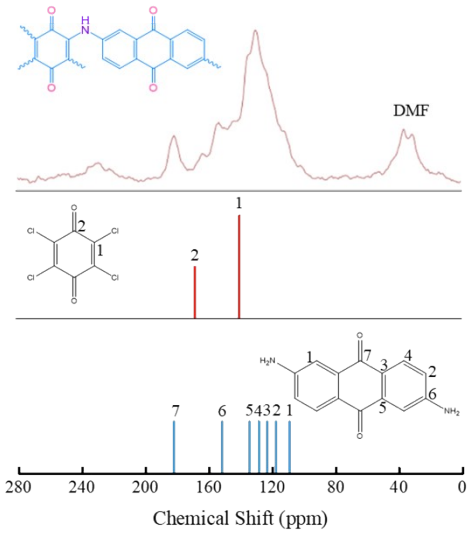

Figure S3. ^{13}C NMR spectra of CMPs unit.

Note to Figure S3: The chemical shift around 30 ppm in ^{13}C NMR spectra of CMPs unit is the solvent peak of DMF, which is more indicative of the conjugated microporous structure of CMPs.

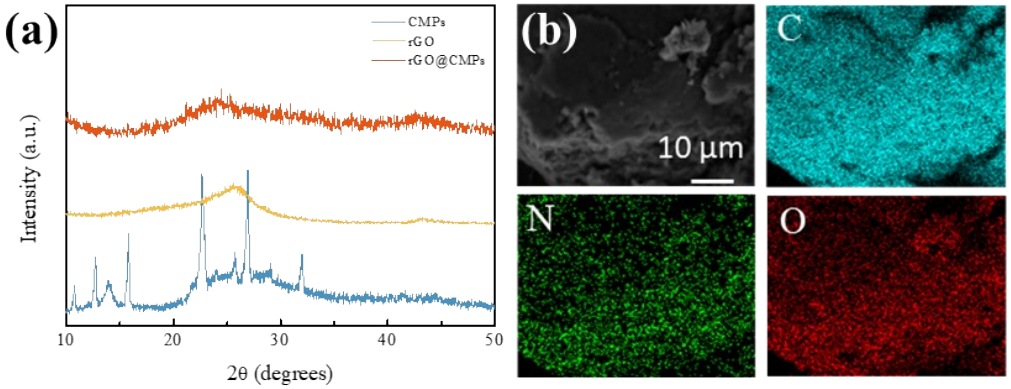

Figure S4. (a) XRD patterns of CMPs. (b) SEM-EDS mapping of rGO@CMPs.

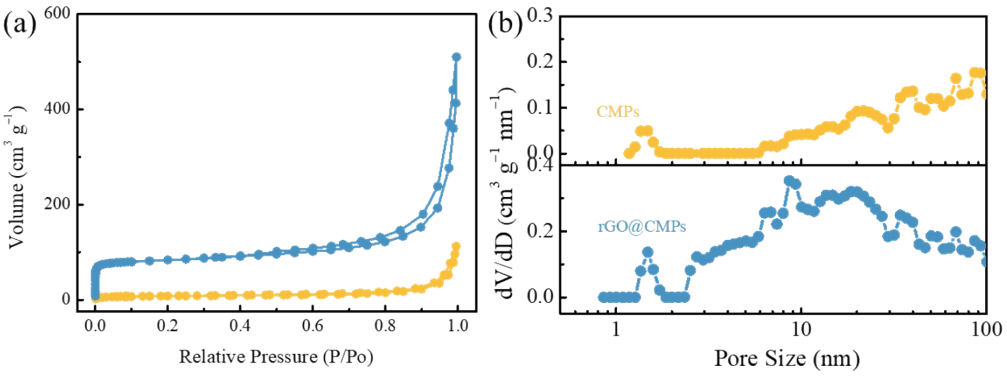

Figure S5. (a) N_2 adsorption-desorption isotherms and (b) the corresponding pore size distribution of CMPs and rGO@CMPs.

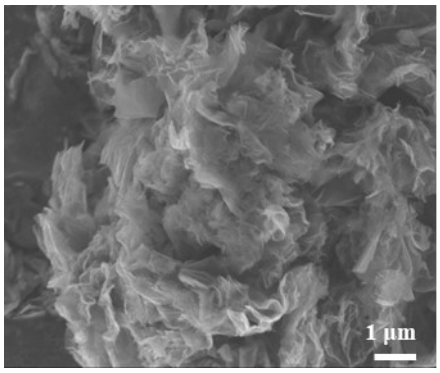

Figure S6. SEM image of rGO@CMPs.

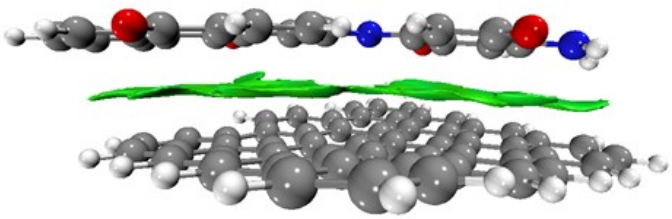

Figure S7. Bimolecular model of rGO and CMPs unit.

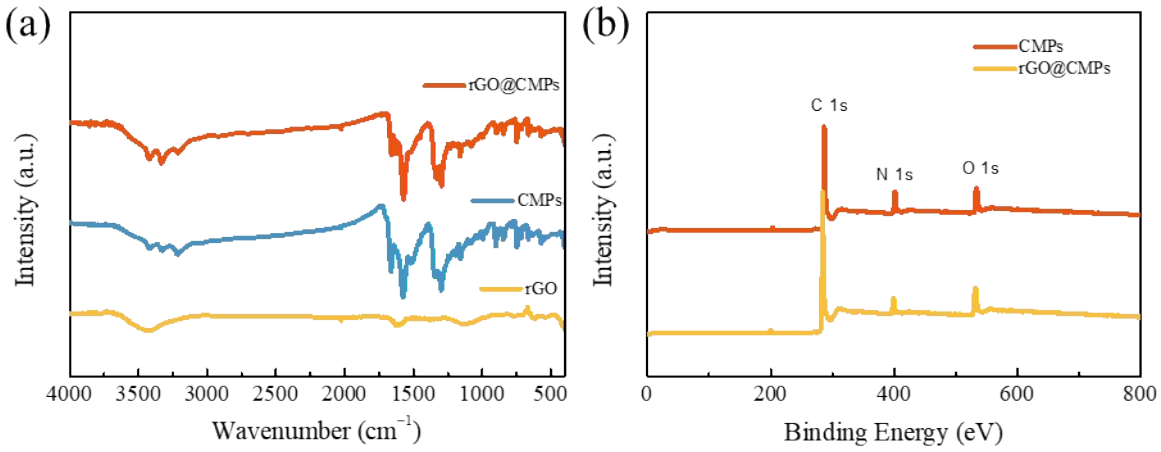

Figure S8. (a) FT-IR spectra and (b) XPS spectra.

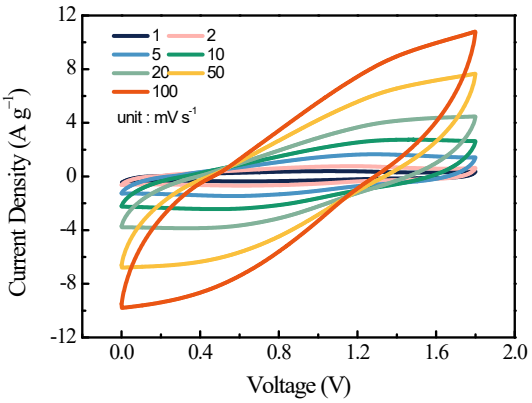

Figure S9. CV curves of rGO at different scan rates.

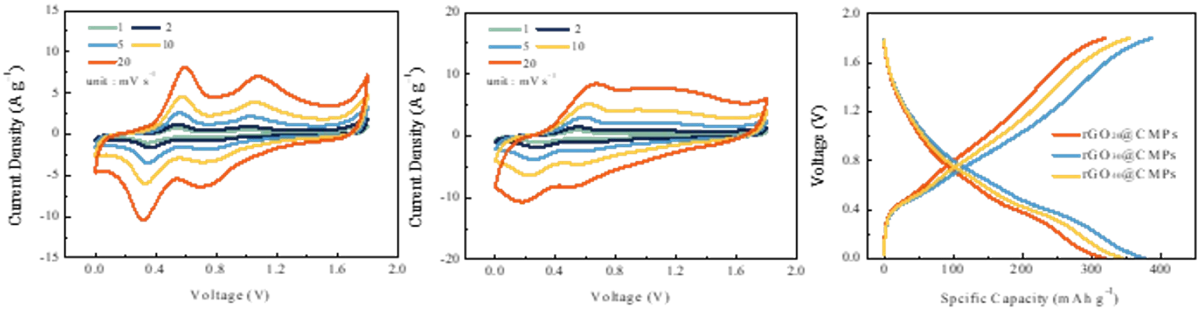

Figure S10. (a, b) CV curves and (c) GCD curves of rGO@CMPs with different mass ratios.

Note of Figure S10: rGO@CMPs with 20% mass ratio rGO doping shows a significant polarization process at high voltage, when the doping amount of rGO reaches a mass ratio of 40%, the CV curves of rGO@CMPs show weak redox activity, indicating that excess rGO buries the electroactive sites of CMPs. Meanwhile, the rGO@CMPs cathode with 30% rGO doping can provide the highest capacity.

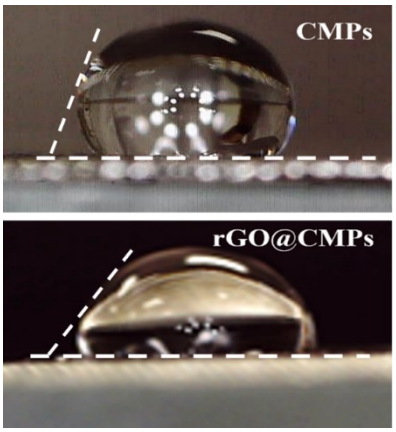

Figure S11. Contact angles of CMPs and rGO@CMPs cathode.

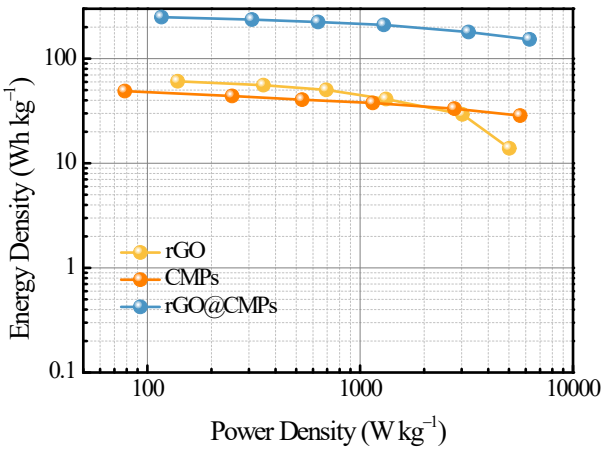

Figure S12. Ragone plots of rGO, CMPs and rGO@CMPs.

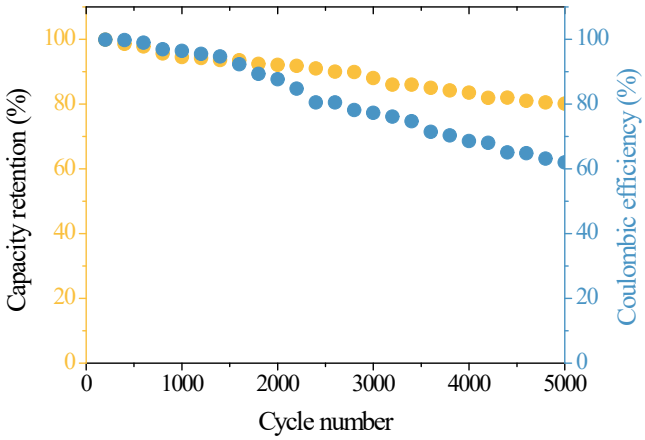

Figure S13. Cycle stability and coulombic efficiency of CMPs.

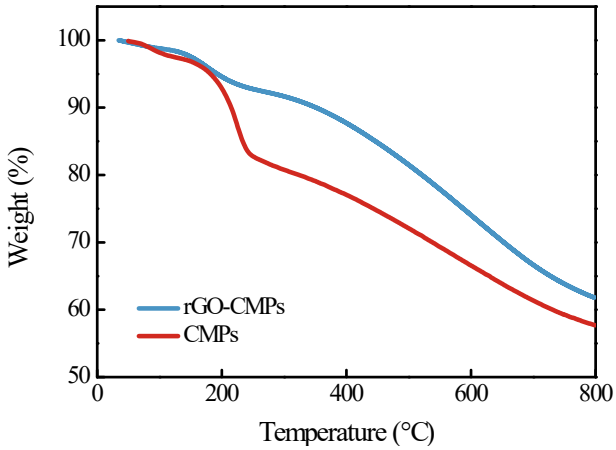

Figure S14. TGA curves of CMPs and rGO@CMPs.

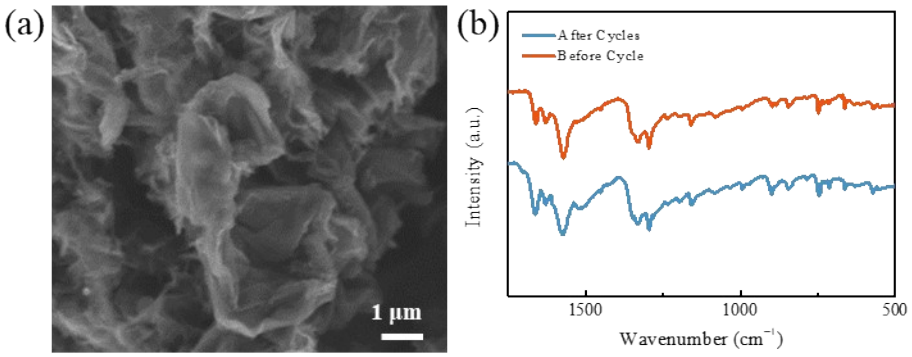

Figure S15. (a) A SEM image and (b) FT-IR spectra of rGO@CMPs cathodes after long-term cycles.

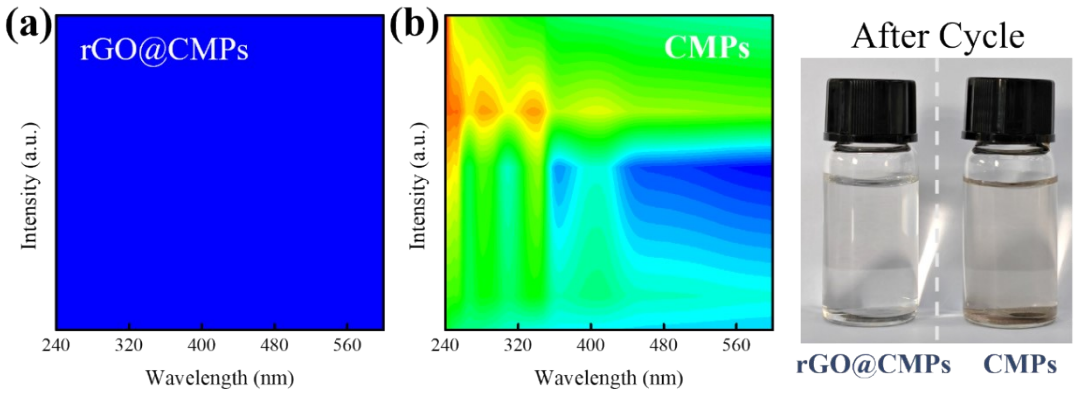

Figure S16. UV-Vis spectra photos of (a) Zn//rGO@CMPs and (b) Zn//CMPs. (c) Photos of rGO@CMP and CMPs electrode immersed in $Zn(CF_3SO_3)_2$ electrolyte after cycling.

Table S1. Comparison of capacity and cycling performance of organic cathodes based ZOBs recently reported in the literatures.

Organic cathodes	Electrolyte	Discharge capacity (mAh g/A g)	Retention (% of no. cycle)	Ref.
DNPT-rGO	3 M $Zn(CF_3SO_3)_2$	150/0.242	94/2000 at 3 A g^{-1}	[S8]
PBQS	3 M $Zn(CF_3SO_3)_2$	203 / 0.02	86/ 50 at 0.04 A g^{-1}	[S9]
PDBS	2 M $ZnSO_4$	260 / 0.1	79 / 2000 at 2 A g^{-1}	[S10]
PPPA	2 M $Zn(CF_3SO_3)_2$	210.2 / 0.05	70.6 /20000 at 5	[S11]

			A g^{-1}	
PANI/CFs	3 M $Zn(CF_3SO_3)_2$	200/0.05	92/3000 at 5 A g^{-1}	[S12]
PDA/CNT	3.3 M $ZnSO_4$	126.2/0.02	96/500 at 0.2 A g^{-1}	[S13]
NQ@CNT	2 M $ZnSO_4$	333.5/0.34	41/1500 at 0.34 A g^{-1}	[S14]
dichlone@CNT	2 M $ZnSO_4$	230.7/0.12	70.9/1000 at 0.118 A g^{-1}	[S14]
APh-NQ@CNT	2 M $ZnSO_4$	202/0.1	67.8/1000 at 0.101 A g^{-1}	[S14]
PQ@AC	2 M $ZnSO_4$	150 / 0.1	96.3/36000 at 5 A g^{-1}	[S15]
rGO@CMPs	2 M $Zn(CF_3SO_3)_2$	378 / 0.2	90.1/25, 000 at 10 A g^{-1}	**This work**

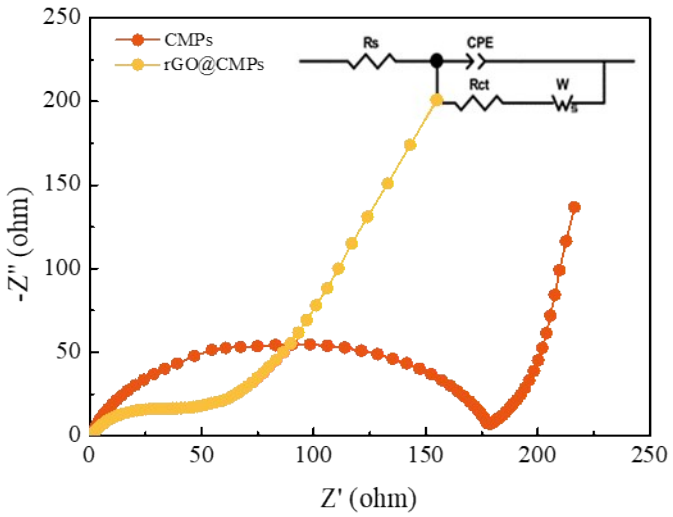

Figure S17. Nyquist plots of CMPs and rGO@CMPs.

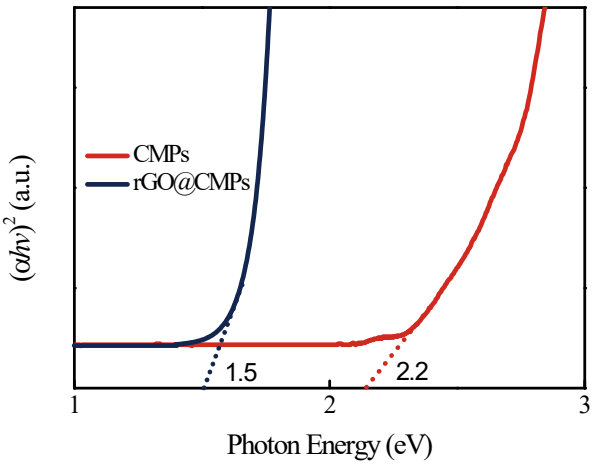

Figure S18. E_g values of CMPs and rGO@CMPs

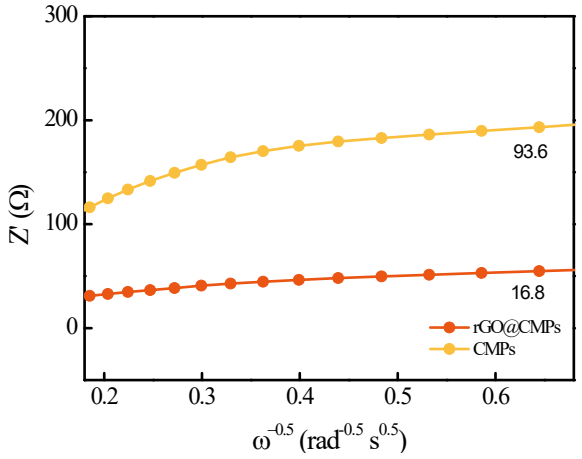

Figure S19. The relationship between Z' and $\omega^{-0.5}$.

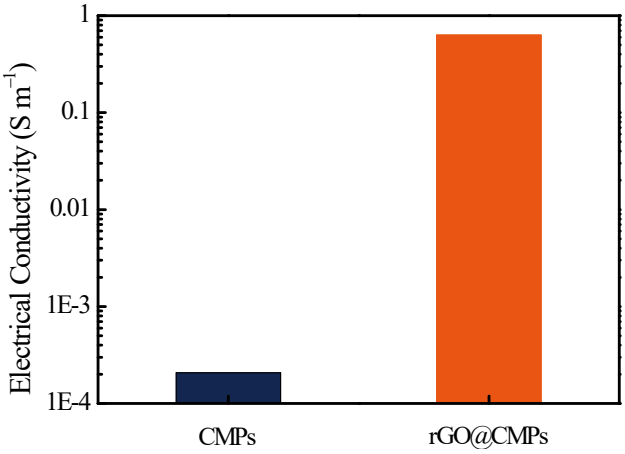

Figure S20. The electrical conductivity of CMPs and rGO@CMPs.

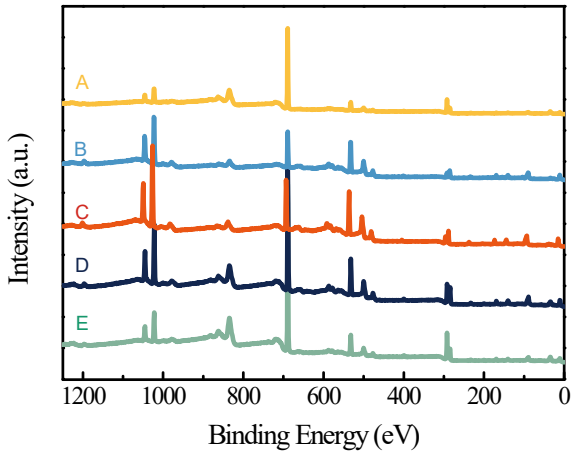

Figure S21. Ex-situ XPS spectra.

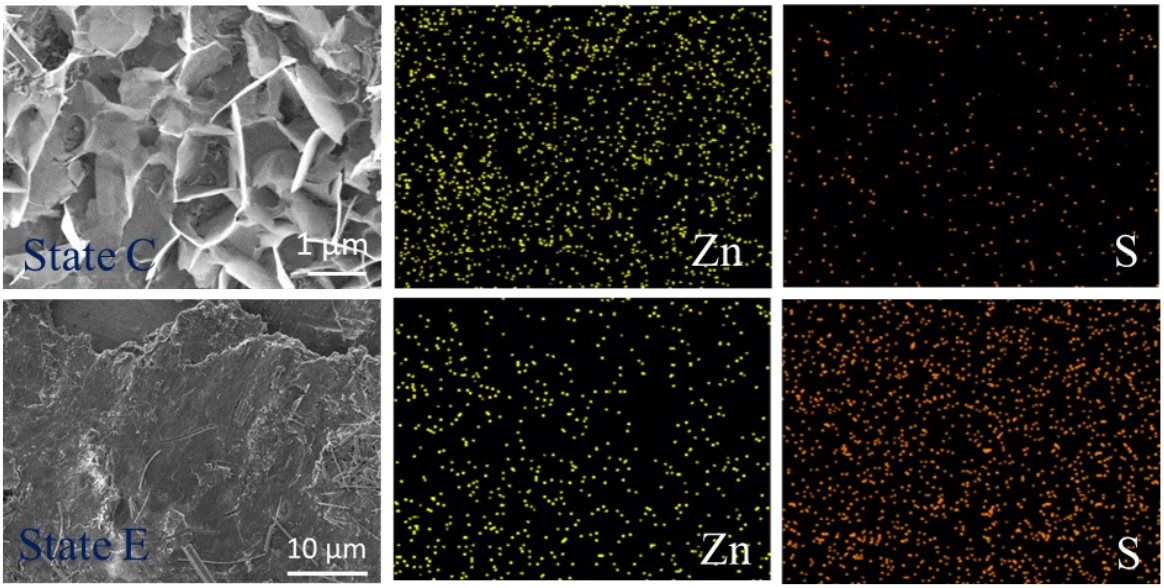

Figure S22. SEM images and EDS-mapping of state C and E.

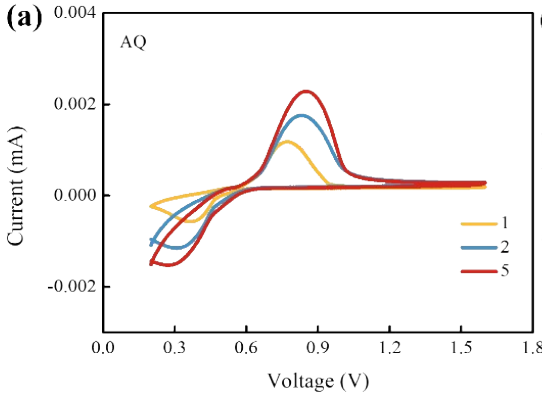

Figure S23. CV curves of AQ.

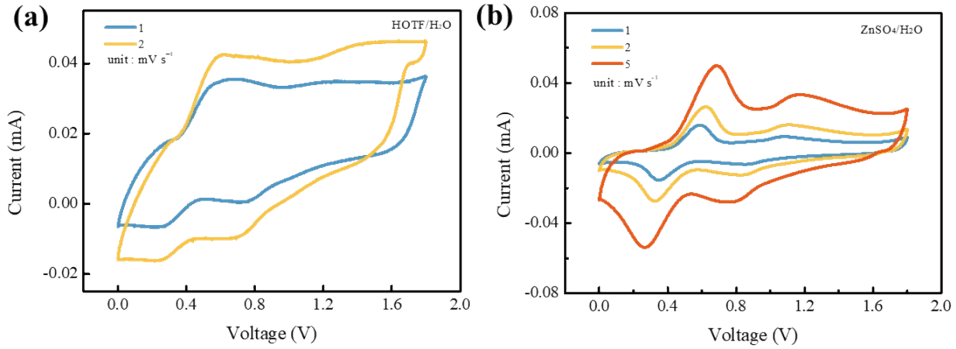

Figure S24. CV curves of rGO@CMPs cathode at (a) HOTF/H_2O and (b) 2 M $ZnSO_4$/H_2O electrolyte.

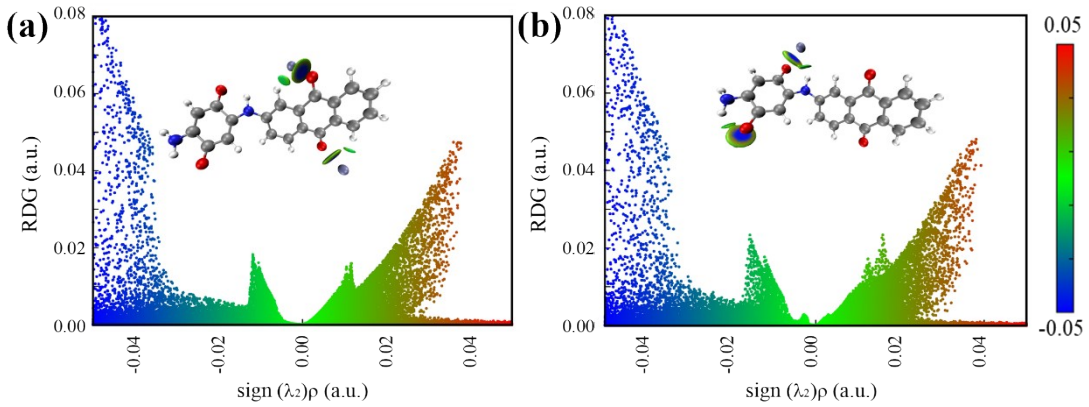

Figure S25. RDG vs. sign(λ_2)ρ plots.

Reference

[S1] H. Yu, B. Zhang, C. Bulin, R. Li, R. Xing, *Sci. Rep-UK* **2016**, 6, 36143.

[S2] C. Long, L. Miao, D. Zhu, H. Duan, Y. Lv, L. Li, M. Liu, L. Gan, *ACS Appl. Energy Mater.* **2021**, 4, 5727.

[S3] Y. Li, G. Wang, T. Wei, Z. Fan, P. Yan, *Nano Energy* **2016**, 19, 165.

[S4] G. W. T. M. J. Frisch, H. B. Schlegel, et al, *Gaussian Inc., Wallingford, CT,* **2016**.

[S5] E. R. Johnson, S. Keinan, P. Mori-Sanchez, J. Contreras-Garcia, A. J. Cohen, W. Yang, *J. Am. Chem. Soc.* **2010**, 132, 6498.

[S6] F. C. T. Lu, *J. Comput. Chem.* **2012**, 33, 580.

[S7] A. D. William Humphrey, and Klaus Schulten, *J. Mol. Graph.* **1996**, 14, 33.

[S8] X. Geng, H. Ma, F. Lv, K. Yang, J. Ma, Y. Jiang, Q. Liu, D. Chen, Y. Jiang, N. Zhu, *Chem. Eng. J.* **2022**, 446, 137289.

[S9] G. Dawut, Y. Lu, L. Miao, J. Chen, *Inorg. Chem. Front.* **2018**, 5, 1391.

[S10] T. Sun, Z. J. Li, Y. F. Zhi, Y. J. Huang, H. J. Fan, Q. Zhang, *Adv. Funct. Mater.* **2021**, 31, 2010049.

[S11] F. Ye, Q. Liu, H. Dong, K. Guan, Z. Chen, N. Ju, L. Hu, *Angew. Chem. Int. Ed.* **2022**, 61, e202214244.

[S12] F. Wan, L. Zhang, X. Wang, S. Bi, Z. Niu, J. Chen, *Adv. Funct. Mater.* **2018**, 28, 1804975.

[S13] X. Yue, H. Liu, P. Liu, *Chem. Commun.* **2019**, 55, 1647.

[S14] J. Kumankuma-Sarpong, S. Tang, W. Guo, Y. Fu, *ACS Appl. Mater. Interfaces* **2021**, 13, 4084.

[S15] B. Yang, Y. Ma, D. Bin, H. Lu, Y. Xia, *ACS Appl. Mater. Interfaces* **2021**, 13, 58818.